Volume 1 | Number 1 | Jan 2013 | Pages 1–100

Journal of
Materials Chemistry A

Materials for energy and sustainability
www.rsc.org/materialsA

Li⁺

ROYAL SOCIETY
OF CHEMISTRY

This is an *Accepted Manuscript*, which has been through the
Royal Society of Chemistry peer review process and has been
accepted for publication.

Accepted Manuscripts are published online shortly after
acceptance, before technical editing, formatting and proof reading.
Using this free service, authors can make their results available
to the community, in citable form, before we publish the edited
article. We will replace this *Accepted Manuscript* with the edited
and formatted *Advance Article* as soon as it is available.

You can find more information about *Accepted Manuscripts* in the
Information for Authors.

Please note that technical editing may introduce minor changes
to the text and/or graphics, which may alter content. The journal's
standard **Terms & Conditions** and the **Ethical guidelines** still
apply. In no event shall the Royal Society of Chemistry be held
responsible for any errors or omissions in this *Accepted Manuscript*
or any consequences arising from the use of any information it
contains.

A Novel Synthesis of Carbon Nanotubes Directly from Indecomposable Solid Carbon Source for Electrochemical Applications

Zhi Zhang[1], Shichun Mu[2], Bowei Zhang[3], Lu Tao[1], Shifei Huang[1], Yizhong Huang[3] and Faming Gao[1], Yufeng Zhao[1]*,

[1]Key Laboratory of Applied Chemistry, Yanshan University, Qinhuangdao, 066004, China.
E-mail: yufengzhao@ysu.edu.cn
[2]State Key Laboratory of Advanced Technology for Materials Synthesis and Processing,
Wuhan University of Technology, Wuhan, 430070, PR China
3School of Materials Science and Engineering, Nanyang Technological University, Nanyang Avenue, 639798, Singapore

Abstract: Carbon nanotubes (CNTs) are synthesized through a novel low cost self-vaporized chemical vapor deposition (SCVD) technique from indecomposable solid carbon source for the first time. This method manipulated to avoid the injecting of flammable gasses, by producing gaseous carbon (e.g. CO) through an in-situ catalyzed gasification of the intermediate product induced by KOH. Simultaneously, the as produced gaseous carbons will deposit on to the pre-imbedded Ni nanocatalyst surface and form CNTs. The growth mechanism is discussed in detail by adjusting the KOH amount. The as-prepared CNTs are rich of oxygen and deficiencies, which endow them with abundant active sites for electrochemical applications. Superior supercapacitor performance is achieved with a specific capacitance 6 times higher than that of commercial CNTs. This technique represents a novel, convenient approach toward large scale production of CNTs directly from solid carbon precursor, and would show promising applications in various industry fields.

Keywords: carbon nanotube, solid carbon source, catalyzed gasification, electrochemical applications

1. Introduction

As a typical one-dimensional nano-sized tubular material, carbon nanotubes (CNTs) have attracted plenty of attention due to their promising applications in numerous fields, such as energy storage, catalysis, electronics and mechanism etc.[1-6] Successful fabrication techniques reported so far mainly include chemical/physical vapor deposition, hydrothermal, electrochemical etching/deposition, laser ablation and electrospinning methods.[7-9] Particularly, chemical vapor deposition (CVD) technique has been extensively investigated due to the mild synthesis condition (such as normal pressure and low growth temperature), high yield, simple facility, and low cost.[10-13] Besides, the wall number, diameter, length, and alignment of as-produced CNTs can be well mediated through CVD technique.[14-17]

However, the traditional CVD processes have one common vital drawback, that explosion is a potential risk, when flushed with the flammable gasses (e.g. methane, acetylene, benzene, xylene, toluene, etc.) as carbon feedstock.[18-21] Thus, a simple alternative route taking solid precursors as carbon source is highly demanded. For example, CNTs can be produced through pyrolysis of solid organo-metallic precursors in vacuum or closed system.[22] Wang et al.[23] synthesized the smallest carbon nanotubes by the pyrolysis of tripropylamine molecules in the channels of porous zeolite $AlPO_4$ single crystals. Chen et al.[24] reported the growth of CNTs using a one-step direct thermolysis of a metal-organic framework. More recently, Tang el at.[25] reported that carbon nanotube/aluminium composite was produced by thermolysis of polyethylene glycol (PEG). These approaches, however involve special solid precursors that can be easily decomposed to form hydrocarbons at low temperature, which limits their applications from mass production.

Herein, we propose a novel large scale synthesis of CNTs through a self-vaporized vapor chemical deposition (SVCD) technique from indecomposable solid carbon source. The cyst shells of Artemia, which is a natural biological crustacean widespread in salt lakes, coastal salt flat pools and other high salt fields all over the world,[26,27] are considered as the ideal solid

carbon precursor. The main composition of the Artemia cyst shell (ACS) is chitosan, therefore the abundant -NH$_2$ and -OH groups on chitosan molecular chains can form complex with some heavy metal ions such as Ni^{2+} etc.,[28-31] which facilitates a uniform pre-imbedding of Ni catalyst into the microstructure of the carbon precursor. This is critical for the homogeneous catalysis during the subsequent growth of CNTs. The fabrication involves a gasification process of the intermediate product catalyzed by KOH and K$_2$CO$_3$, through which gaseous carbons such as CO are produced and deposited on to the Ni catalyst surface to form CNTs. It is conceived to be an environmentally friendly, convenient and safe synthesis method without using any hazardous reductant gas. The as prepared CNTs are multiwalled with high oxygen content, and denoted as O-MCNTs. The unique microstructure endows O-MCNTs with abundant active sites and improved wettability, showing great potential for the application in electrochemical field.

2. Experimental Section

Materials: Artemia cyst shells were attained from Chinese Academy of Aquaculture and Sciences. All chemicals used here were of analytical grade. Potassium hydroxide (KOH, Kermel Tianjin Chemical Co. Ltd., China), hydrochloric acid (HCl, Kermel Tianjing Chemical Co. Ltd., China) and nickel acetate ((Ni (CH$_3$COO)$_2$·4H$_2$O, Guangfu Tianjin Chemical Reagent Co. Ltd., China) were used without further purification. The commercial multiwall carbon nanotubes were purchased from Beijing DK Nano Technology Co. Ltd., China.

Synthesis of Ni imbedded in graphitic porous carbon frameworks (Ni-GPCFs): The Ni-GPCFs is synthesized shown as follows: 1.2g Artemia cyst shell powder was first impregnated with 100 mL aqueous solution containing 1.2g nickel acetate and magnetic stirred for 6h, followed by sonication of 30 min for uniform dispersion. After that, 3.6 g KOH was added to the above mixture with stirring and heated to 80 °C to form a Ni^{2+}/ACS/KOH paste. Finally, the paste was carbonized, activated and graphitized at 800 °C for 2 h at a

heating rate of 2 °C min^{-1} in flowing Ar atmosphere. After cooling to room temperature, the final sample was repeatedly washed with HCl (1 mol L^{-1}) solution and deionized water, respectively, to remove impurities, and then freeze-dried under vacuum at -120 °C.

Synthesis of O-MCNTs: The as-prepared Ni-GPCF was mixed with KOH with a weight ratio of $W_{KOH}/W_{Ni\text{-}GPCF}$ = 5:1 in an agate mortar. The obtained mixture was then heated to 850 °C at a heating rate of 10 °C min^{-1} in Ar atmosphere, and held there for 2 h. Similar processes were also performed at different $W_{KOH}/W_{Ni\text{-}GPCF}$ of 1:1, 2:1, 3:1, 4:1 and 6:1, respectively. In order to remove the residue of nickel, the as obtained sample was washed with HCl (1 mol L^{-1}) aqueous solution and deionized water for several times repeatedly, and then dried at 120 °C for 12 h.

Materials Characterization: The morphology and structure of the samples were characterized by scanning electron microscopy (SEM, Carl Zeiss SUPRA 55 SAPPHIRE, 15 kV), transmission electron microscopy (TEM, JEM-ARM 200F, 200 kV) and Raman spectroscopy (WITec, alpha300R, excited by a 532 nm laser). X-ray diffraction (XRD) measurements were carried out by Rigaku D/MAX-2500 powder diffractometer with Cu-Kα radiation (λ= 0.154 nm) operated at 40 kV, 200 mA. The variation of the chemical structure was confirmed by Fourier transform infrared spectrometer (FTIR, NiCOLET IS10). X-ray photoelectron spectrum (XPS) was conducted on a Thermo Scientific ESCALAB 250Xi photoelectron spectrometer using Mg-Kα as the exciting source (1253.6 eV). Nitrogen adsorption-desorption isotherms were obtained on an ASAP 2020 HD88 (Micromeritics Instrument Corporation) instrument at 77 K. The electrical conductivity was measured with a ST-2722 semiconductor powder resistivity apparatus (Suzhou Jingge Electronic technology Co. Ltd., China).

Electrochemical Tests: The capacitive performance of the as prepared samples was evaluated with a three-electrode system. The working electrodes were prepared by mixing active materials, acetylene black, and 5 wt% polyvinylidene fluoride (PVDF) at a weight ratio of

85:10:5 in N-methylpyrolidinone (NMP) solvent, coating on Pt net ($1x1$ cm^2) current collector

and drying in a vacuum oven. The counter electrode and reference electrode are platinum foil

and saturated calomel electrode (SCE), respectively. The cyclic voltammetry (CV) and

electrochemical impedance spectroscopy (EIS) tests were carried out on a CHI 660E

workstation (Chenhua, China). Galvanostatic charge/discharge (GCD) tests were performed

by computer controlled cycling equipment (Land CT2001A, China). All the electrochemical

tests were performed in 1 M H_2SO_4 aqueous solution. The specific capacitance of the O-

MCNTs electrode or the commercial Multiwall Carbon electrode was calculated from the

GCD curves based on the following equation:

$$Cs = \frac{I}{m\frac{dV}{dt}}$$

Equation (1)

where I (A) is the discharge current, m (g) is the mass of active materials, $\frac{dV}{dt}$ represents the

slope of discharge curves, respectively.

3. Result and Discussion

Figure 1 demonstrates the morphology and microstructure of as-prepared sample. SEM

and TEM images (**Figure 1a-c**) reveal the remarkably uniform shape of the tube-like products,

with diameters ranging from 45 to 60 nm and lengths of up to several micrometers. The

selected area electron diffraction patterns (SAED) indicate their high crystallinity character

(**Figure 1d**). The high-resolution TEM (HRTEM) image (**Figure 1e**) shows clearly narrow

hollow tube cavities (<10nm) with thick tube walls (>20nm), generating a structure in which

the graphitic walls are parallel to the tube axis ("straight and hollow" form). The

discontinuous lattices reveal the intermittent arranged carbon atoms, indicating the abundant

defects formed during crystallization. The graphitic structures of the carbon walls are further

confirmed by XRD and Raman analysis. The characteristic peaks in XRD patterns (**Figure 1f**)

could be indexed as the (002) (100), (101) and (004) crystal facets of graphite phase

respectively (JCPDS no. 75-0444).[24] The relatively wide full width at half maximum (FWHM) of 0.653 implies the deteriorated degree of crystallinity,[32] which is in good agreement with the HRTEM data. A representative Raman spectrum of the carbonized sample (the inset in **Figure 1f**) shows two bands centered at 1588.7 (G band) and 1357.8 cm^{-1} (D band), corresponding to the graphitic carbon phase with sp^2 electronic configuration and the presence of amorphous or disordered carbon, respectively. The relatively high I_D/I_G intensity ratio of 0.809 (the inset in **Figure 1f**), indicates the large portion of sp^3 carbon atoms at defect sites.[33,34] On the other hand, XPS (**Figure 1g**) and FTIR (**Figure 1h**) characterizations confirm the rich of oxygen functional groups of the as-prepared O-MCNTs, and a total 23.7 at% oxygen content is revealed from the XPS survey spectrum (**Figure 1g**). In addition, a vibrational band at 1633 cm^{-1} from FTIR spectrum (**Figure 1h**) is typical for a stretching mode of OH group in an enol C=C-OH form, which should be attributed to the simultaneous KOH etching during the reaction.[35] It is worth to note that the C-O (286.48 ev) and C=O (288.7 eV) fractions in O-MCNTs reach up to 13.49% and 9.2%, respectively, according to the curve fitting of C1s spectrum (**Figure S1**, Supporting Information).

To explore the growth mechanism of the CNTs, the microstructure of the carbon precursor and the intermediate product was characterized (**Figure 2**). The overall fabrication process of O-MCNTs is illustrated in **Scheme 1 a**. Briefly, the ACS was is as the carbon source (**Figure 2a**).[36-38] The ACS is firstly soaked with aqueous solution containing Ni^{2+} ions, these Ni^{2+} ions will then bond to the free -NH$_2$ groups or -OH groups of forming Ni^{2+}-chitosan metal chelate (**Scheme 1b**),[28] and thus Ni^{2+} ions can be uniformly anchored to the ACS. A dilute aqueous KOH solution is then added, and the OH$^-$ ions will react with Ni^{2+} immediately, leading to the precipitation of Ni(OH)$_2$ nanoparticles (**Equation 2**). The above complex is preheated at 80

$$Ni(CH_3CO_2)_2 \bullet 4H_2O \xrightarrow{\text{Impregnation}} Ni^{2+} \xrightarrow{\text{KOH}} Ni(OH)_2 \qquad \textbf{Equation (2)}$$

^{o}C to remove the residue water and provide a homogenous distribution of Ni(OH)$_2$ nanoparticles within the ACS architecture. The as obtained product is then calcined in Ar atmosphere at 800 ^{o}C, where Ni(OH)$_2$ is converted to Ni metal catalyst, and ACS is carbonized and graphitized, forming intermediate product composed of petaliform graphitic porous carbon with Ni imbedded in the frameworks (Ni-GPCF) (**Figure 2b**). The XRD patterns (**Figure 2c**) prove the co-existence of graphitized carbon (JCPDS no.41-1487) and metallic Ni phase (space group: Fm-3m(225), JCPDS no. 65-2865). **Figure 2d** and **2e** demonstrate that metallic Ni nanoparticles (NPs) with size of 30-45 nm are uniformly imbedded in carbon framework, which will further serve as the catalyst for CNT growth. The uniform particle size and homogeneous distribution of Ni catalyst could be attributed to the constraint effect of the hierarchical porous microstructure of the ACS. As comparison, Ni catalysts were imbedded into chitosan powders following the same procedure, and CNTs with ununiformed morphologies were obtained due to the inhomogeneous distribution of Ni particles (**Figure S2**, Supporting Information). Moreover, the lattice fringes with interplanar distance of 0.176 nm are assigned to the (100) facets of an fcc nickel nanocrystal (**Figure 2e**), which is in good agreement with the XRD patterns (**Figure 2c**). These exposed Ni (100) facets are reported as more active than the Ni (111) facet for CNTs growth.[39] While the graphitic nanoribbons around Ni NPs (**Figure 2e**), would act as the nucleation cores for the growth of O-MCNTs. The SEM image and the corresponding energy-dispersive X-ray spectrometry (EDS) mapping images of C, O and Ni elements (**Figure 2g-j**), clearly demonstrate the uniform distribution of Ni NPs in the intermediate product.
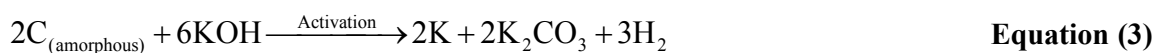
It is reported that there are two main growth mechanisms of CNTs.[40,41] One possible mechanism is through the formation of intermediate metastable nickel carbide such as NiC$_x$ or Ni$_3$C etc., and then release the dissolved carbon to form CNTs.[41] The other is through the direct decomposition of hydrocarbons (e.g. CH$_4$, C$_2$H$_2$, etc.) or carbon monoxide (CO) over the catalysts nanoparticles surfaces (e.g. transmission metal or their alloys etc.) as presented

by Baker et al.[40] In this mechanism, the interaction of carbon molecules with the metal surface is limited to certain crystal facets, and thus different crystallographic orientations of catalysts particles will lead to the formation of different CNT morphologies. In order to get detailed information during the reaction, we conducted an experiment to investigate the phase transformation behavior by immediately cooling down to room temperature from $850^{o}C$, instead of holding there for 2h, the TEM images of the as obtained products are shown in **Figure 3**. **Figure 3a** clearly shows that the graphitic shells around the Ni NPs are transferred into the tube walls at some highly active sites, indicating the graphitic carbon phase act as the nucleation cores during the growth of O-MCNTs. Three types of CNTs with different morphologies are observed in the same sample, which should represent three different precipitation models according to the previous study.[40] In **Figure 3b**, rhombic shaped Ni particle is encapsulated within one single CNT, which generates a geometric shape containing six well-defined crystallographic facets of Ni (the left inset in **Figure 3b**). The nanostructures are established by a bidirectional mode in which the CNTs are precipitated simultaneously from four facets of Ni NPs, while other two facets (front and back, the right inset in **Figure 3b**) are capable of dissolving carbon atoms. Therefore, the tube walls of CNTs in this growth mode is inclined at an angle to the tube axis. In contrast, **Figure 3c** demonstrates that graphite tube walls are precipitated from only a single face of the particle, which emerge at the end of tubes, and several faces where precipitation of carbon in the form of concentric graphite platelets. As a consequence, the CNTs are hollow and the tube walls are parallel to the tube axis (**Figure 3c**). The growth of CNTs in **Figure 3d** also follows a bidirectional mode (the inset in **Figure 3b**), where individual Ni particle is encapsulated in the tube, suggesting that the diameter of as-prepared O-MCNTs is determined by the size of nickel particles. However, there are four facets that are capable of dissolving carbon atoms, and only two facets are available for precipitating carbon, compared with the first model (**Figure 3b**). So, the graphite platelets are stacked in a direction perpendicular to the CNTs

axis. As a result, CNTs with non-hollow structure would be obtained through this reaction

model, which is consistent with the TEM results (**Figure 3d**). Therefore, the growth

mechanisms of three different CNT morphologies corresponding to the three models

presented by Baker et al,[40] co-existed in the reaction, indicating the direct deposition

mechanism, in which the decomposed gaseous carbons (hydrocarbons or carbon monoxide)

are deposited directly on the catalysts surface. Meanwhile, no nickel carbide phases are

observed in this product, further proving the direct deposition process. Note that, uniform

morphology of O-MCNTs is achieved for the final product (**Figure 1**), which is straight with

narrow inner hollow space. This could be explained by the nanocrystal reconstruction of Ni

catalyst during the holding time at $850^{\circ}C$.[42,43] For the reaction without holding time at high

temperature, three types of Ni catalysts compete to exist in the initial age of forming CNTs,

inducing growth of CNTs with different morphologies; while the catalyst metals achieve well-

defined crystallographic orientations, after holding 2h at $850 \, ^{\circ}C$,[44,45] which finally leads to the

formation of uniform shaped CNTs.

　　Concerning no gaseous carbons are injected during the whole fabrication process, the origin

of the reaction gas for further CNT growth remains an unresolved puzzle. Note that, KOH can

react with carbon at high temperature to form K_2CO_3, (**Equation 3**), while using K_2CO_3 or

KOH as catalyst for the gasification of coals to produce CO and H_2 is a well known

reaction.[46,47] In this condition, we can assume reasonably that the gases (CO, H_2 and CO_2 etc.)

produced through above reactions (**Equation 3** and **4**) would serve as the carbon feedstock for

$$2C_{(amorphous)} + 6KOH \xrightarrow{\text{Activation}} 2K + 2K_2CO_3 + 3H_2 \qquad\qquad \textbf{Equation (3)}$$

$$C + K_2CO_3 \xrightarrow{\text{Catalyzed gasification}} 2CO + 2K_2O \qquad\qquad \textbf{Equation (4)}$$

the growth of CNTs through a vapor deposition process. Therefore, in this mechanism, KOH

plays a critical role by etching the amorphous carbon preferentially around the graphitic

nanoribbons and then providing carbon feedstock gas for the CNT deposition through a

catalyzed gasification reaction, which is defined as a catalyzed gasification and self-vaporized chemical vapor deposition (SCVD) process. Besides, the presence of H_2 produced in the reactions (**Equation 3**) is essential to obtain straight and hollow CNTs rather than other growth conformations,[48,49] which is consistent with the SEM and TEM results (**Figure 1**). Furthermore, this H_2 gas can also prevent the carbon stacking on the nickel surface, avoiding the catalyst deactivation problem during the synthesis process.[50]

To further verify this proposed mechanism, additional experiment was performed by adjusting the weight ratio between KOH and Ni-GPCF ($W_{KOH}/W_{Ni-GPCF}$). No CNTs were produced when the ratio of $W_{KOH}/W_{Ni-GPCF}$ equals to 1 (**Figure S3**, Supporting Information), attributed to the inadequate gas produced from the catalyzed gasification for the CVD process with low KOH concentration. With increased $W_{KOH}/W_{Ni-GPCF}$ ratio, the amount of CNTs produced increases gradually attributed to more gaseous carbon (**Figure 4b-d**) produced as carbon feedstock. All the carbons are transformed to CNTs when $W_{KOH}/W_{Ni-GPCF}$ increased to 5:1 (**Figure 1a**) and 6:1 (**Figure 4d**). However the CNT yield for the latter sample is significantly reduced due to the etching of CNTs by the excessive KOH. Therefore, mass production of CNTs directly from biomass can be realized through this novel technique with the careful control of KOH and catalyst amount.

The high content of oxygen and deficiencies on O-MCNTs are favorable for electrochemical applications by supplying more active sites for energy storage or anchoring nanoparticles.[51,52] To evaluate the possible application of O-MCNTs in electrochemical field, the as prepared sample was directly applied as supercapacitor electrode without any further modification, and tested in a three-electrode system in 1M H_2SO_4 electrolyte. The supercapacitor performances were evaluated by means of cyclic voltammetry (CV), electrochemical galvanostatic charge/discharge (GCD) test, and compared with the commercial CNTs. **Figure 5a** shows the typical CV curves of as-prepared O-MCNTs and commercial CNTs at a scan rate of 5 mV s^{-1} within a potential range of 0 to 1 V (vs. SCE). In

detail, a pair of extremely symmetrical redox peaks appears on the CV curve of O-MCNTs, which would contribute Faradic capacitance due to the oxygen-containing groups. In contrast, the commercial MCNTs sample exhibited negligible CV area, indicating the significantly lower capacitance values, compared with O-MCNTs. The GCD curves (**Figure 5b**) exhibits a slight deviation from linearity, demonstrating the pseudocapacitive behavior of O-MCNTs. The specific capacitance (SC) is calculated from discharge curves (**Equation 4**, see Experimental Section), a high SC value of 122 F g^{-1} is achieved for O-MCNTs at current density of 0.2 A g^{-1}, which is 6 times higher than that of commercial CNTs (18 F g^{-1}, **Figure 5b**). **Figure 5c** shows the shape of CV curves can be finely maintained at scanning rate ranging from 5 to 1000 mV s^{-1}, indicating good rate performance of the as produced O-MCNTs. This is also confirmed by GCD results (**Figure S4**), which demonstrates a capacitance retention of 78% from 0.2 to 2 A g^{-1} (**Figure 5d**).

The electrochemical impedance spectroscopy (EIS) was carried out with the perturbation amplitude of 5 mV at the frequency range of 10^{-2}-10^{5} Hz, to investigate the electrical resistance responses of O-MCNTs and commercial CNTs. Both the EIS plots consist of a quasi-semicircle in the high-frequency region, and a nearly vertical line at the low-frequency region (**Figure 5e**). In the high-frequency region of Nyquist curves (inset in **Figure 5e**), the first intercept along the real axis represents the equivalent series resistance (ESR), the diameter of the quasi-semicircle corresponds to the charge transfer resistance (CTR) and the slope at low-frequency region reflects the ion diffusive resistivity at electrode/electrolyte interface. Both the ESR and the CTR of O-MCNTs are slightly larger than those of the commercial CNTs, which should be attributed to the decreased electronic conductivity caused by the large number of doped oxygen atoms and deficiencies on O-MCNTs. The conductivity test (**Figure S6**, Supporting Information) also confirmed this result. However, the O-MCNTs exhibit a more vertical straight line than that of commercial CNTs in the low-frequency region, suggesting its ideal capacitive behavior and the lower electrolyte diffusion

11

resistance.[53] This could be related to the improved wettability of electrolyte towards electrode surface by doping of heteroatoms[53] (**Figure S8**, Supporting Information). Generally, the rich of oxygen-functional groups is often accompanied with sacrificed cyclability.[54] The long cycle performance of O-MCNTs is evaluated using the galvanostatic charge-discharge technique conducted at 2 A g^{-1} (**Figure 5f**). Only 3% capacitance deteriorates for O-MCNTs over 10000 cycles, revealing an outstanding electrochemical stability. The good long cycle life for the O-MCNTs indicates that, the in-situ introduced heteroatoms on carbon frameworks during the synthesis process, are more stable under harsh working conditions, compared with those introduced through post-treatments.[36]

The significantly improved capacitance behavior can be explained by the unique microstructure of the as prepared O-MCNTs. In comparison with the commercial CNTs, the O-MCNTs exhibit much better wettability (**Figure S8**, Supporting Information) due to the oxygen doping and discontinuous defects, which can effectively enhance the surface utilization and facilitate easy ion entrance and diffusion[56,57] (**Figure 6**). Besides, these doped oxygen atoms on the carbon skeleton (**Figure 6**) can greatly increase the Cs value by introducing a large portion of pseudocapacitance through redox reaxtions.[55] Specifically, the pseudocapacitance (C_p) of O-MCNTs at 0.2 A g^{-1}, is calculated as 78 F g^{-1} according to T_p (the discharge time of the pseudocapacitance) by extending the linear part of the discharge curve to X-axis (**Figure S5,** Supporting Information),[55] demonstrating a totally 64% of the total C_s. Meanwhile, O-MCNTs demonstrate a much higher specific surface area (124.2 m^2 g^{-1}) than that of commercial CNTs (82.1 m^2 g^{-1}, **Figure S7a**, Supporting Information), contributing enhanced double-layer capacitance. Therefore, the unique structural feature of O-MCNTs is more favorable for capacitive behavior by offering better utilization of the electroactive surface area, more electroactive sites and enhanced ion transformation kinetics. Note that, the as prepared O-MCNTs without further modification present superior specific

capacitance and cycling stability as compared to the CNTs, and even comparable with those doped CNTs reported in previous works (**Table 1**).

4. Conclusions

In this work, we report a novel strategy for mass-producible fabrication of oxygen rich carbon nanotubes from solid biomass carbon source via a novel self-vaporized chemical vapor deposition process. A possible mechanism and discussed in detail, in which the KOH plays a critical role by etching the amorphous carbon preferentially of the graphitized intermediate product, and then providing carbon feedstock gas (e.g. CO) for the CNT deposition through a catalyzed gasification reaction. The yield of the CNTs can be tuned by adjusting the amount of KOH added. The as-prepared CNTs possess high oxygen content, leading to 6 times of enhanced specific capacitance as compared to commercial CNTs, accompanied with superior long cycle life. This technique may be applied to produce CNTs through other solid materials, as long as the metal catalysts can be uniformly loaded into the carbon precursors.

Acknowledgments

References

[1] J. M. Schnorr and T. M. Swager, Chem. Mater., 2011, 23, 646-657.

[2] R. V. Noorden, Nature, 2014, 507, 26-28.

[3] H.Wu, G. Chan, J. W. Choi, I. Ryu, Y. Yao, M. T. McDowell, S. W. Lee, A. Jackson, Y. Yang, L. Hu and Y. Cui, Nat. Nanotechnol., 2012, 7, 310-315.

[4] P. Zhou, X. Yang, L. He, Z. M. Hao, W. Luo, B. Xiong, X. Xu, C. J. Niu, M. Y. Yan, and L. Q. Mai, Applied Physics Letters, 2015, 106, 111908.

[5] E.W. Wong, P. E. Sheehan and C. M. Lieber, Science, 1997, 277, 1971-1975.

[6] C. Wang, M. Waje, X. Wang, J. M. Tang, R. C. Haddon and Y. S. Yan, Nano Lett., 2004, 4, 345-348.

[7] F. Yang, X. Wang, D. Q. Zhang, J. Yang, D. Luo, Z. W. Xu, J. K. Wei, J. Q. Wang, Z. Xu, F. Peng, X. M. Li, R. M. Li, Y. L. Li, M. H. Li, X. D. Bai, F. Ding and Y. Li, Nature, 2014, 510, 522-524.

[8] Y. Qin, S. M. Lee, A. L. Pan, U. Gösele and M. Knez, Nano Lett., 2008, 8, 114-118.

[9] R. K. Joshi and J. J. Schneider, Chem. Soc. Rev., 2012, 41, 5285-5312.

[10] L. He, M. Toda, Y. Kawai, H. Miyashita, M. Omori, T. Hashida, R. Berger and T. Ono, Microsystem Technologies, 2014, 20, 201-208.

[11] D. H. Zhang, M. H. Miao, H. T. Niu, and Z. X. Wei, ACS Nano, 2014, 8, 4571-4579.

[12] D. H. Zhang, Y. L. Wu, T. Li, Y. Huang, A. Q. Zhang and M. H. Miao, ACS Appl. Mater. Interfaces, 2015, 7, 25835-25842.

[13] Z. L. An, L. He, M. Toda, G. Yamamoto, T. Hashida and T. Ono, Nanotechnology, 2015, 26, 195601.

[14] Q. Zhang, J. Q. Huang, W. Z. Qian, Y. Y. Zhang and F. Wei, Small, 2013, 9, 1237-1265.

[15] W. M. Zhu, A.Borjesson and K. Bolton, Carbon, 2010, 48, 470.

[16] Y. B. Yan, J. W. Miao, Z. H. Yang, F. X. Xiao, H. B. Yang, B. Liu and Y. H. Yang, Chem. Soc. Rev., 2015, 44, 3295-3346.

[17] S. B. Sinnott, R. Andrews, D. Qian, A. M. Rao, Z. Mao, E. C. Dickey and F. Derbyshire, Chem. Phys. Lett., 1999, 315, 25-30.

[18] Y. Wang, F. Wei, G. H. Luo, H. Yu and G. S. Gu, Chem. Phys. Lett., 2002, 364, 568-572.

[19] D. Venegoni, P. Serp, R. Feurer, Y. Kihn, C. Vahlas and P. Kalck, Carbon, 2002, 40, 1799-1807.

[20] Y. J. Tian, Z. Hu, Y. Yang, X. Z. Wang, X. Chen, H. Xu, Q. Wu, W. J. Ji and Y. Chen, J. Am. Chem. Soc., 2004, 126, 1180-1183.

[21] H. Li, D. He, T. Li, M. Genestoux and J. Bai, Carbon, 2010, 48, 4330-4342.

[22] C. N. R. Rao and A. Govindaraj, Acc. Chem. Res., 2002, 35, 998-1007.

[23] N. Wang, Z. K. Tang, G. D. Li and J. S. Chen, Nature, 2000, 408, 50-51.

[24] L. Y. Chen, J. F. Bai, C. Z. Wang, Y. Pan, M. Scheer and X. Z. You, Chem. Commun., 2008, 13, 1581-1583.

[25] J. Tang, G. Fan, Z. Li, X. Li, R. Xu, Y. Li, D. Zhang, W. J. Moon, S. D. Kaloshkin and M. Churyukanova, Carbon, 2013, 55, 202-208.

[26] S. F. Wang and S. C. Sun, Microsc. Res. Tech., 2007, 70, 663-670.

[27] P. Sorgeloos, E. Bossuyt, E. Lavina, M. Baeza-Mesa and G. Persoone, Aquaculture, 1977, 12, 311-315.

[28] D. Ravi, P. A. J. Antony, K. K. Anoop, K. V. J. Alex and R. Rajesh, Int. Sci. Tech. Res., 2012, 1, 43-50.

[29] X. Q. Sun, B. Peng, Y. Ji, J. Chen and D. Q. Li, AIChE Journal, 2009, 55, 2062-2069.

[30] J. A. R. Filho, E. E. Bach, R. R. Vargas, D. A .W. Soares and A. A. A. D. Queiroz, Journal of Applied Polymer Science, 2004, 92, 1310-1318.

[31] A. Shanmugapriya, M. Hemalatha, B. Scholastica and A. P. T. Augustine, Der Pharma Chemica, 2013, 5, 141-155.

[32] A. Dandekar, R.T.K. Baker and M.A. Vannice, Carbon, 1998, 36, 1821-1831.

[33] K. A. Wepasnick, B. A. Smith, K. E. Schrote, H. K. Wilson, S. R. Diegelmann and D. H. Fairbrother, Carbon, 2011, 49, 24-36.

[34] M. Q. Zhao, Q. Zhang, X. L. Jia, J. Q. Huang, Y. H. Zhang and F. Wei, Adv. Funct. Mater., 2010, 20, 677-685.

[35] D. Yang, G. Q. Guo, J. H. Hu, C. C. Wang and D. L. Jiang, J. Mater. Chem., 2008, 18, 350-354.

[36] Y. F. Zhao, W. Ran, J. He, Y. F. Song, C. M. Zhang, D. B. Xiong, F. M. Gao, J. S. Wu and Y. Y. Xia, ACS Appl. Mater. Interfaces, 2015, 7, 1132-1139.

[37] Y. F. Zhao, Z. Zhang, Y. Q. Ren, W. Ran, X. Q. Chen, J. S. Wu and F. M. Gao, J. Power Sources, 2015 286, 1-9.

[38] Y. F. Zhao, W. Ran, J. He, Y. Z. Huang, Z.F. W. Liu, Y. F. Tang, D. W. Gao and F. M. Gao, Small, 2015, 1310-1319.

[39] B. Louis, R. Vieira, A. Carvalho, J. Amadoua, M. J. Ledouxa and C. Pham-Huua, Topics in Catalysis, 2007, 45, 75-80.

[40] N. M. Rodriguez, A. Chambers and R. T. K. Baker, Langmuir, 1995, 11, 3862-3866.

[41] C. W. Huang, H. C. Wu, W. H. Lin and Y. Y. Li, Carbon, 2009, 47, 795-803.

[42] W. Moritz, R. Imbihl, R. J. Behm, G. Ertl and T. Matsushima, J. Chem. Phys., 1985, 83, 1959-1968.

[43] K. Müller, Progress in surface science, 1993, 42, 245-255.

[44] Q. X. Wang, Q. Zhang, L. P. Chen, L. Y. Yu and L. F. Dong, Journal of Materials Science & Technology, 2014, 30, 917-921.

[45] F. Y. Cao, Q. Jiang, Y. Fang, S. G. Ban, S. S. Ou, H. X. Qian and Y. Zhao, Applied Surface Science, 2013, 283, 958-962.

[46] H. L. Zhu, X. M. Wang, J. G. Zhang, K. Yao, G. S. Yu and X. J. Wang, Energy Technology, 2015, 3, 961-967.

[47] S. R. Kelemen, H. Freund and C. Mims, [C]//ABSTRACTS OF PAPERS OF THE AMERICAN CHEMICAL SOCIETY. 1155 16TH ST, NW, WASHINGTON, DC 20036: AMER CHEMICAL SOC, 1985, 189(APR): 22-FUEL.

[48] R. L. V. Wal and L. J. Hall, Carbon, 2003, 41, 659-672.

[49] C. Park and R. T. K. Baker, J Phys Chem B, 1998, 5168-5177.

[50] C. Pham-Huu, R. Vieira, B. Louis, A. Carvalhoc, J. Amadoua, T. Dintzer and M. J. Ledouxa, Journal of Catalysis, 2006, 240, 194-202.

[51] A. Schierz and H. Zanker, Environ Pollut., 2009, 157, 1088-1094.

[52] H. H. Cho, K. Wepasnick, B. A. Smith, F. K. Bangash, D. H. Fairbrother and W, P. Ball, Langmuir, 2009, 26, 967-981.

[53] H. Y. Liu, H. H. Song, X. H. Chen, S. Zhang, J. S. Zhou and Z. K. Ma, Journal of Power Sources, 2015, 285, 303-309.

[54] P. Simon and Y. Gogotsi. Nat. Mater., 2008, 7, 845-854.

[55] X. Q. Yang, D. C. Wu , X. M. Chen and R. W. Fu, J. Phys. Chem. C, 2010, 114, 8581-8586.

[56] J. Zhao, H. W. Lai, Z. Y. Lyu, Y. F. Jiang, K. Xie, X. Z. Wang, Q. Wu, L. J. Yang, Z. Jin, Y. W. Ma, J. Liu and Z. Hu, Advanced Materials, 2015.(DOI: 10.1002/adma.201500945)

[57] L. Li, R. M. Li, S. L. Gai, P. Gao, F. He, M.L. Zhang, Y. J. Chen and P. P. Yang, J. Mater. Chem. A, 2015, 3, 15642-15649.

[58] N. Halonen, J. Maklin, A.-R. Rautio, J. Kukkola, A. Uusimaki, G. Toth, L. M. Reddy, R. Vajtai, P. M. Ajayan and K. Kordas, Chemical Physics Letters 2013, 583, 87-91.

[59] Z. Niu, W. Zhou, J. Chen, G. Feng, H. Li, W. Ma, J. Li, H. Dong, Y. Ren and D. Zhao, Energy Environ Sci, 2011, 4, 1440-1446.

[60] L. Li, R. M. Li, S. L. Gai, P. Gao, F. He, M. L. Zhang, Y. J. Chen and P. P. Yang, J. Mater.Chem. A, 2015, 3, 15642-15649.

[61] S. J. He, H. Q. Hou and W. Chen, Journal of Power Sources, 2015, 280, 678-686.
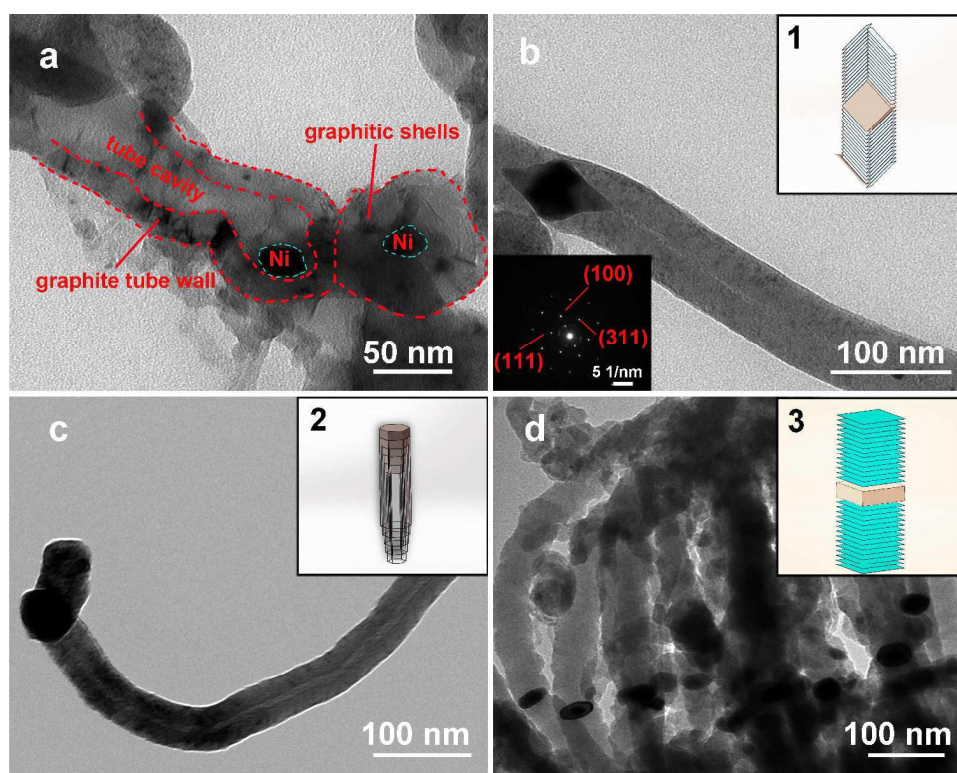
Figures
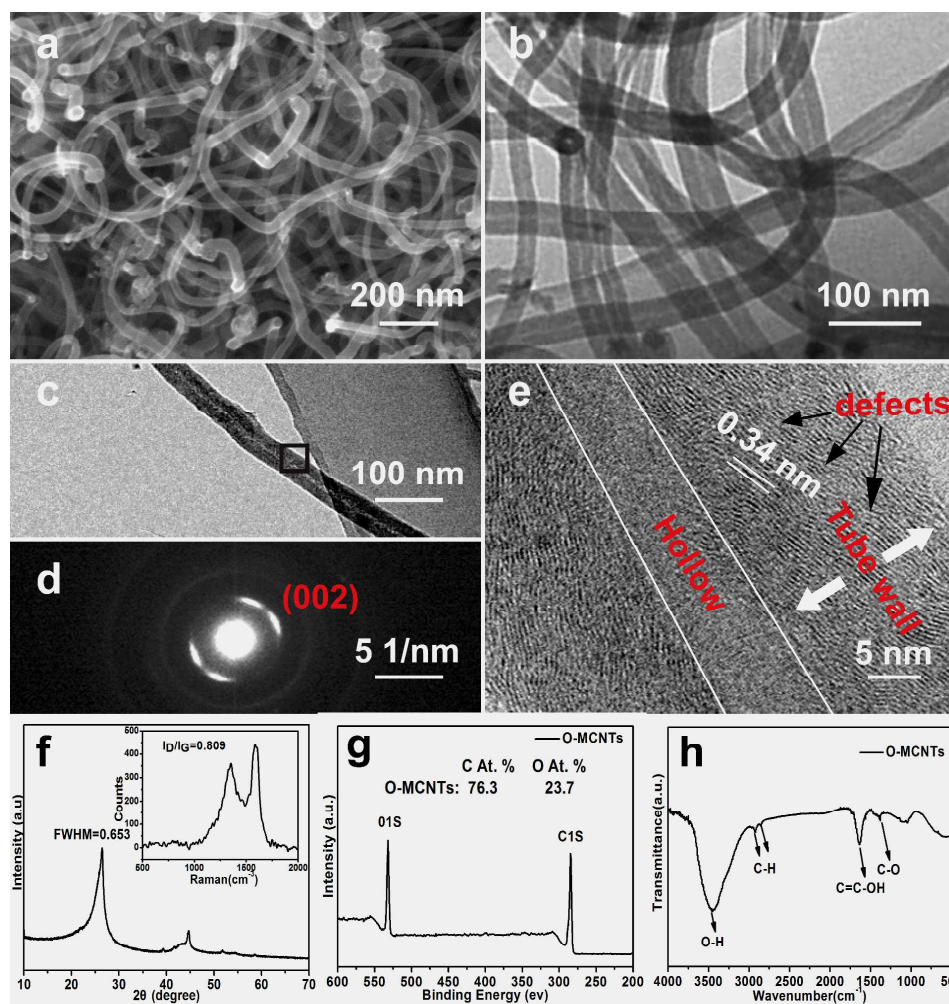
Figure 1. (a) SEM images and (b-c) TEM images; (d) the SEAD pattern; (e) HRTEM corresponding to the black box area in (c); (f) XRD pattern, the inset shows the Raman spectrum of O-MCNTs; (g) An X-ray photo spectroscopic (XPS) broad scan spectrum (200-600eV); (h) FT-IR spectra of O-MCNTs.
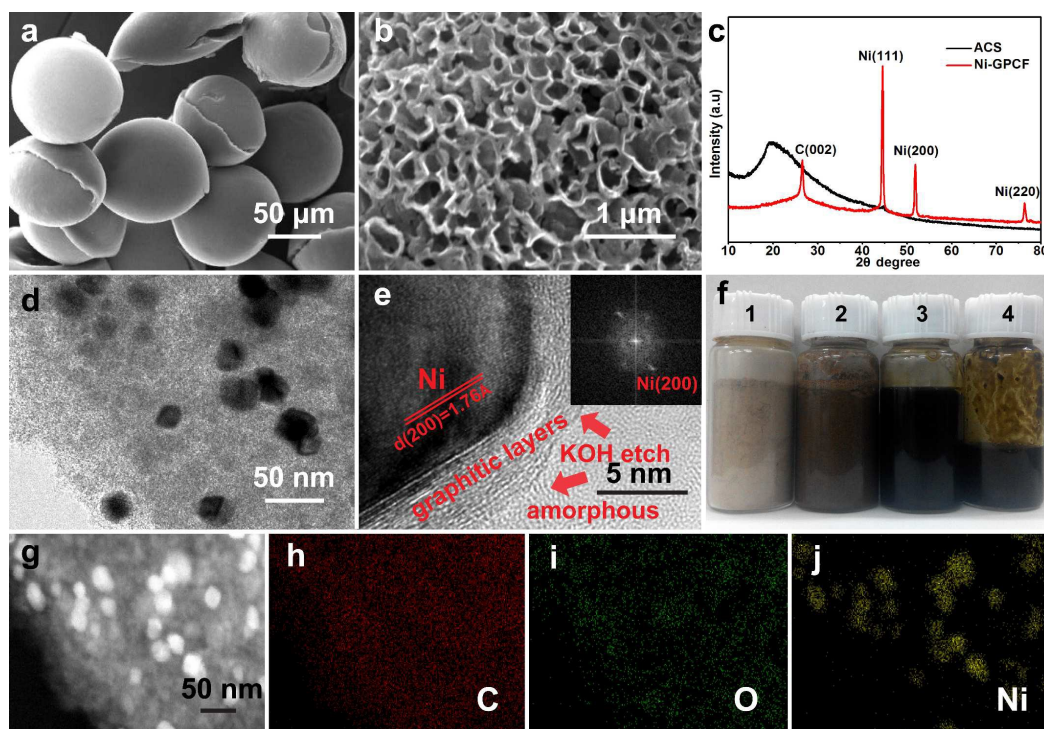
Figure 2. SEM image of (a) ACS temple; (b) Ni-GPCF; (c) XRD pattern of ACS and Ni-GPCF; (d) TEM image of Ni-GPCF; (e) HRTEM of Ni particle embedded in graphitized carbon. The inset shows SAED of Ni particle; (f) Photography of the preparation of Ni-GPCF: 1: ACS temple, 2: ACS impregnated with Ni salt solution, 3:nickel-ion-anchored ACS by KOH, 4: preheated nickel-ion-anchored ACS/KOH mixture; (g) SEM image of Ni-GPCF; and the corresponding EDS mapping of: C (h), O (i) and Ni (j).

Figure 3. TEM images of CNTs with different morphologies produced without holding time at 850°C; and inset: schematic show of the structural relationship between the catalyst particle and graphite tube walls with the different precipitation pattern during the growth of CNTs.
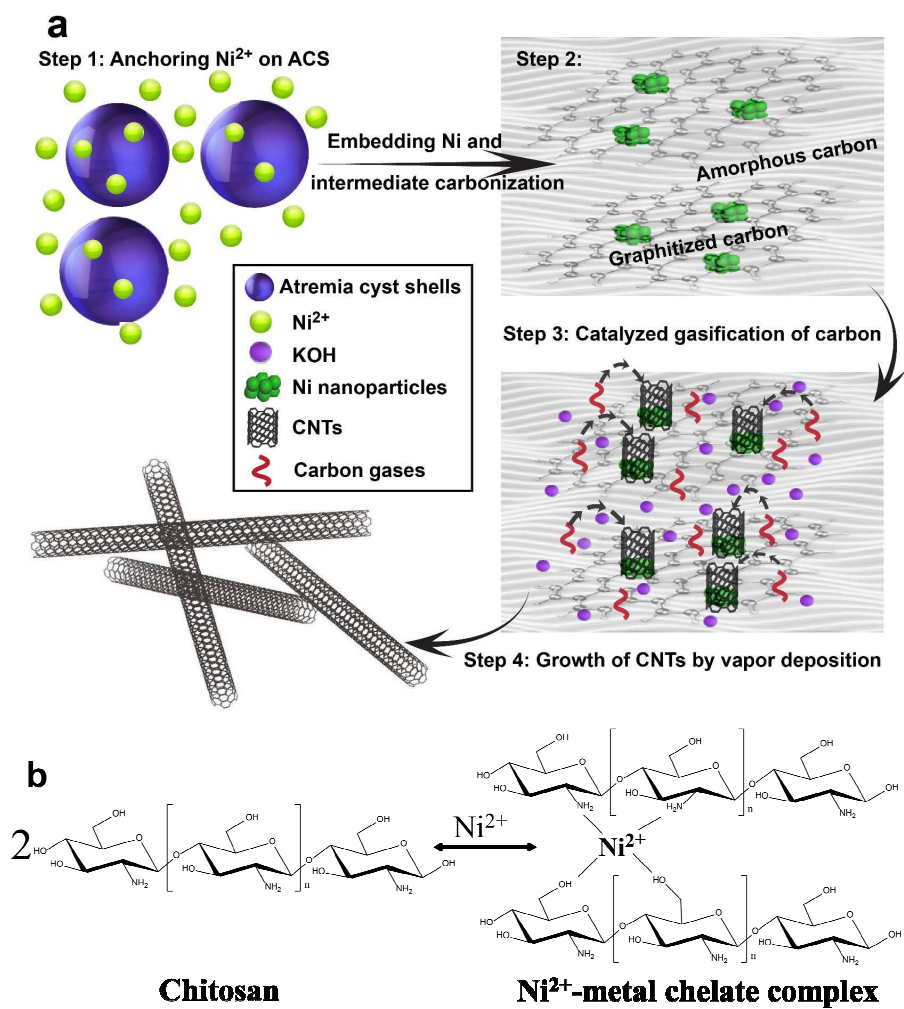
Scheme 1. a, Schematic illustration of CNTs growth; b, Ni^{2+} ions can penetrate into the

matrix of chitosan to form metal chelate complex.
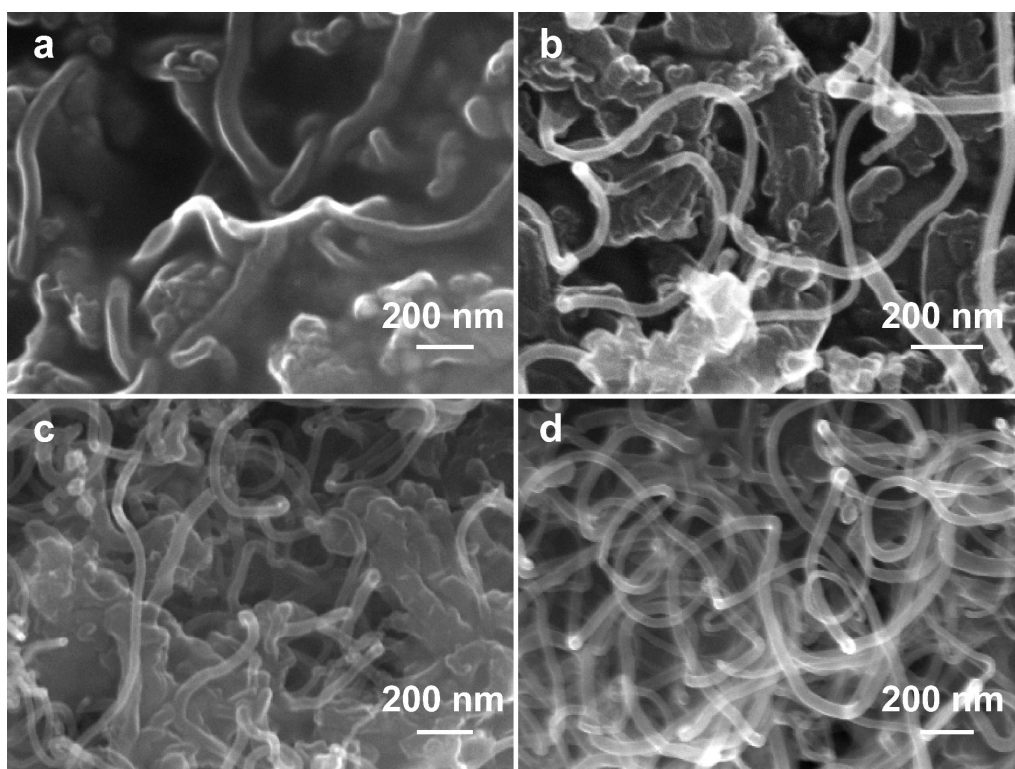
Figure 4. SEM images of the as-synthesized O-MCNTs from Ni-GPCF with different weight

ratios ($W_{KOH}/W_{Ni\text{-}GPCF}$): (a) 2:1; (b) 3:1; (c) 4:1 and (d) 6:1.
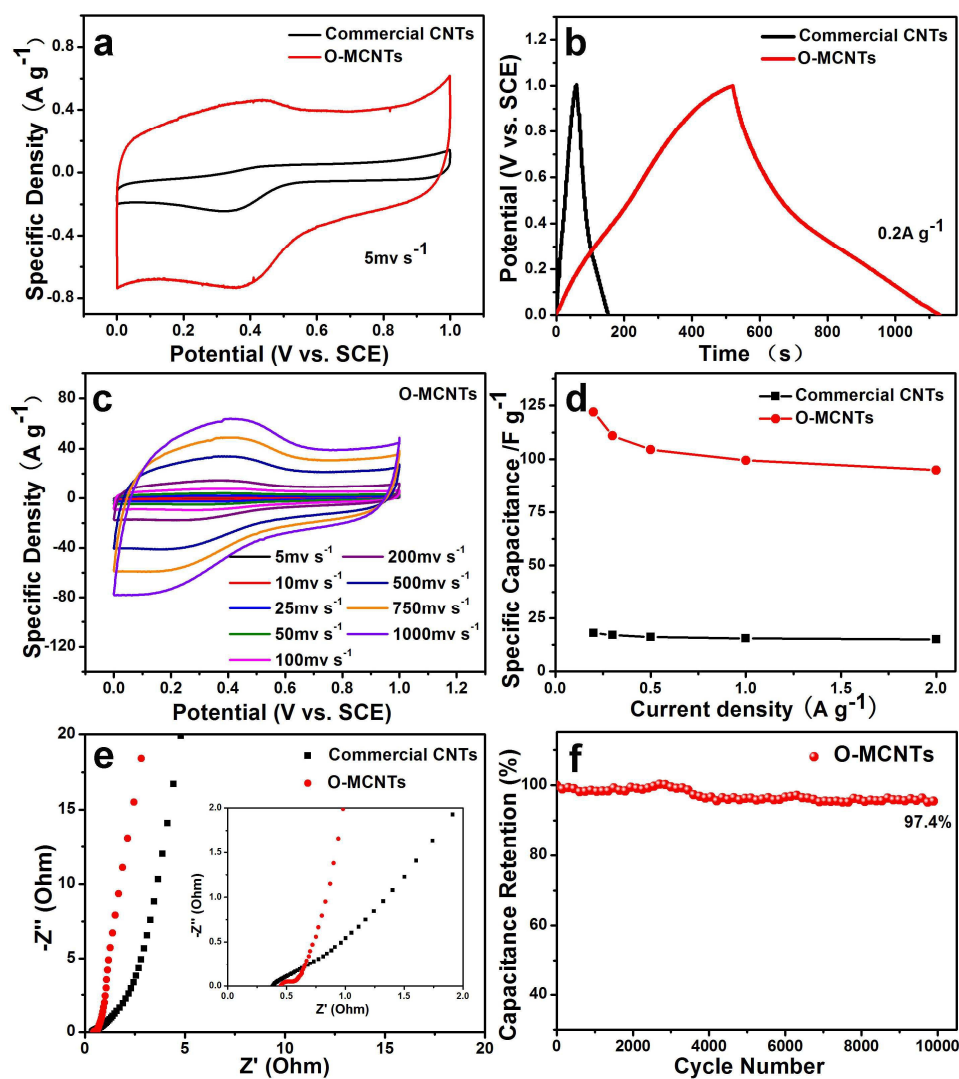
Figure 5. (a) CV curves of commercial CNTs and O-MCNTs samples at a scanning rate of 5 mV s^{-1} in 1 M H$_2$SO$_4$ aqueous solution; (b) Galvanostatic charge/discharge curves of the as prepared samples at 0.2 A g^{-1}; (c) CV curves of O-MCNTs measured with a voltage of 1V at various scanning rates; (d) Specific capacitance versus current density from 0.2 A g^{-1} to 2 A g^{-1} of the commercial CNTs and O-MCNTs; (e) Nyquist plots of commercial CNTs and O-MCNTs within the range of 10^{-2} Hz ~10^{5} Hz; (f) Long-term cycle performance of O-MCNTs at 2 A g^{-1}.
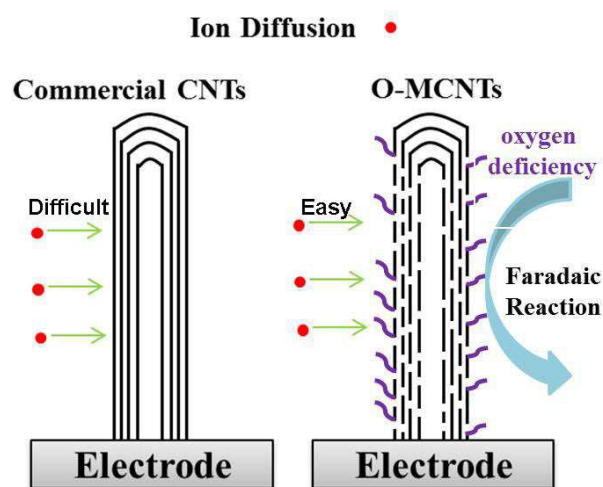
Figure 6. Schematic model comparing the ion diffusion and faradaic reaction for commercial CNTs and O-MCNTs.

Table 1. Comparison of the C_s and cycling stability of O-MCNTs and some carbon nanotubes from previous works.

Sample	Voltage window (V)	Electrolyte	Capacitance measured at	C_s (F g^{-1})	Cycling Stability	Ref
MWCNT	0.7	6 M KOH	0.05 v s^{-1}	29	----	58
SWCNT	3	1 M LiClO$_4$	0.75 A g^{-1}	35	----	59
CNT	0.8	1 M Na$_2$SO$_4$	1 A g^{-1}	15	----	60
N-doped CNTs	0.8	1 M Na$_2$SO$_4$	1 A g^{-1}	120	87% (8 A g^{-1}, 4000 cycles)	60
P-doped CNTs/CF	0.9	6 M KOH	0.5 A g^{-1}	133	95% (50 A g^{-1}, 5000 cycles)	61
O-MCNTs	1	1M H$_2$SO$_4$	0.2 A g^{-1}	122	97% (2 A g^{-1}, 10000 cycles)	This work

The Table of Contents Entry

Carbon nanotubes (CNTs) are firstly synthesized through a novel low cost self-vaporized chemical vapor deposition (SCVD) technique. This technique represents a novel, convenient approach toward large scale production of CNTs directly from indecomposable solid carbon source.